IET Generation, Transmission & Distribution

Research Article

IET Journals
The Institution of Engineering and Technology

Distance protection algorithm for multiterminal HVDC systems using the Hilbert–Huang transform

ISSN 1751-8687
Received on 15th October 2019
Revised 23rd March 2020
Accepted on 9th April 2020
E-First on 20th May 2020
doi: 10.1049/iet-gtd.2019.1551
www.ietdl.org

Vinícius Albernaz Lacerda[1] ✉, Renato M. Monaro[2], David Campos-Gaona[3], Denis V. Coury[1], Olimpo Anaya-Lara[3]*

[1]*Department of Electrical and Computer Engineering, S ao Carlos School of Engineering, University of S ao Paulo, Av. Trabalhador S ao-carlense, 400, São Carlos, Brazil*

[2]*Department of Electric Energy and Automation Engineering, Polytechnic School, University of São Paulo, Av. Prof. Luciano Gualberto, Travessa 3, 158, São Paulo, Brazil*

[3]*Department of Electronic and Electrical Engineering, University of Strathclyde, 16 Richmond St, Glasgow, Scotland*

**Current affiliation: Visiting Researcher at the Department of Electronic and Electrical Engineering, University of Strathclyde, 16 Richmond St, Glasgow, Scotland.*

✉ *E-mail: vinicius.albernaz.freitas@usp.br*

Abstract: Multiterminal high-voltage direct current (HVDC) systems still need advances in terms of protection in order to improve their reliability. In this context, the distance protection can play a major role by adding selectivity to the existing DC fault detection algorithms. Hence, the present work proposes a non-unit DC distance protection algorithm that uses the frequency of the DC voltage transient oscillation to estimate the distance of the fault. The DC voltage transient frequency is extracted using the Hilbert–Huang transform and compared with a pre-defined frequency/distance curve. The technique was evaluated by simulating faults in a four-terminal symmetric monopole multiterminal HVDC system. In the simulation environment the algorithm was fully selective for faults within the first protection zone and had a correct operation rate of 94% or more for faults located in the second protection zone. To further validate the presented technique, the proposed algorithm was embedded in a digital signal controller, running in real-time. In all performed tests in hardware, the faults were correctly detected and identified as being internal or external. The results indicate that the proposed algorithm could be used in real-world applications, in conjunction with fault detection techniques, adding selectivity to multiterminal DC protection schemes.

1 Introduction

Power transmission systems are facing new challenges in recent years, due to the expansion of modern AC grids. Some examples are the submarine transmission, the interconnection of asynchronous systems, the energy supply in isolated systems and the interconnection of renewable sources [1, 2].

In this context, high-voltage direct current (HVDC) transmission through voltage-source converters (VSCs) is being viewed as a feasible solution to overcome these challenges [3] due to its high controllability and capacity to build meshed grids. However, high-power multiterminal DC grids still require substantial advances from the existing point-to-point HVDC technology. The two major challenges are the grid control and protection [4].

Regarding protection, components such as circuit breakers and protection algorithms need to be improved [5, 6]. As the converters capacitors discharge at the first moment of the fault, short-circuit currents in DC grids are high, and the algorithms must detect and identify the fault within a reduced time window [7].

DC fault detection can be done fast and straightforwardly using travelling waves and derivative-based algorithms [8–12]. However, there is still a need to selectively identify the cable in fault and localise the short-circuit [13]. This cable protection coordination is one of the major challenges for multiterminal DC protection systems [14]. In [15], the faulted line is identified using a triple criteria: undervoltage, voltage derivative and current derivative. The algorithm operated fast and without communication, but no results for faults beyond the protected line and no noise sensitivity tests were shown. In [16], fault detection is performed using the voltage across the DC fault-current-limiting reactor. The fault detection is fast but no line identification is proposed and communication is used as backup protection for high-resistive faults. In [17], the faulted line is identified by a fuzzy system that uses the wavelet decomposition energies of the DC current, but the method was only tested for radial multiterminal systems with 2-level converters. Recent studies [18–20] have proposed using the fault transient information to detect the fault and identify the faulted line without communication, but no additional information is available in terms of fault distance.

Unlike AC systems where the distance is estimated using the impedance [21, 22], in DC systems the absence of frequency precludes the calculation of the reactance, which imposes complexities in finding the location of the DC faults.

Recent studies contour the calculation of impedance using other system variables. In [23] a distance protection technique is proposed for DC cables used in wind energy systems. The technique estimates the fault distance using a ratio of the measured voltage drop between two known locations and the distance between them. However, the technique loses confidence for high-fault resistances and it was applied to short cables only. In [24] the fault distance is estimated resolving the differential equations of the frequency-dependent model of the protected cable. The algorithm could estimate the distance with a low error. However, the algorithm makes use of a 15 ms time window, which makes it unfeasible for use in primary DC grids protection. In [25] the travelling waves natural frequencies were used to locate faults in a line commutate converter (LCC)-HVDC system. The algorithm located faults with less than 0.3% error. However, the algorithm was proposed for point-to-point connections and was not analysed in multiterminal VSC-HVDC systems. In [26], an AC voltage is generated by a full-bridge MMC and the estimated line reactance is used to localise the fault. The algorithm used a reduced sampling time, however, the proposed fault location scheme takes tens of ms to localise the fault, which is way beyond DC breakers' critical time. Hence, there is a lack of techniques that can estimate the distance of the fault in multiterminal HVDC systems, without

Table 1 Comparison between the proposed protection algorithm and previous distance protection algorithms

	Time window	Topology	No. of terminals	Cables length
[23]	_a	DC wind farm	multiterminal	short
[24]	15 ms	LCC-HVDC	2	long
[25]	10 ms	LCC-HVDC	2	long
[26]	> 40 ms	MMC-HVDC	2	medium
proposed method	4 ms	MMC-HVDC	multiterminal	long

[a]Sample by sample.

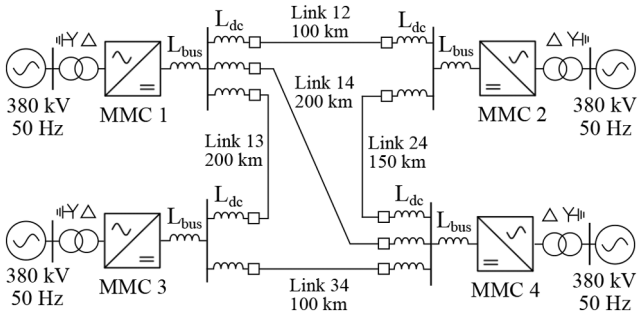

Fig. 1 *MTDC system single-line diagram [29]*

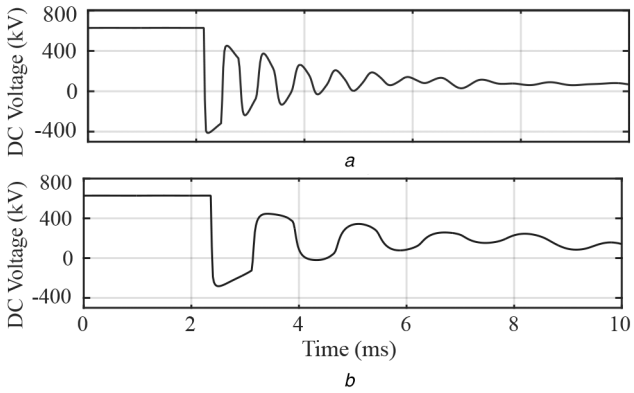

Fig. 2 *DC voltage behaviour in time during a 1 Ω pole-to-pole fault in the MTDC system*
(a) Fault distance 30 km, ***(b)*** Fault distance 70 km

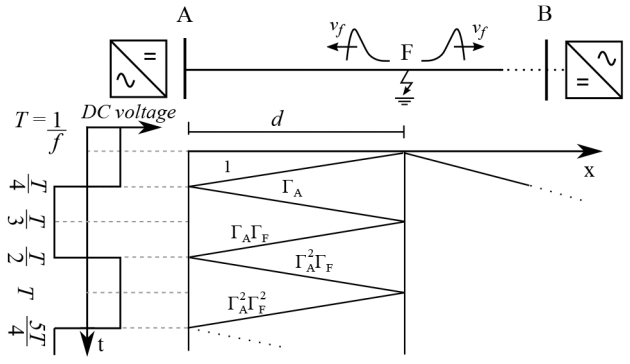

Fig. 3 *Lattice diagram*

communication between terminals, using a short time window. The method has the benefit of not requiring new sensors, as in [27], or communication, as in [28]. Table 1 summarises the advantages of the proposed method compared to previous distance protection algorithms.

Therefore, this work proposes a distance protection algorithm that uses the frequency of the DC voltage to estimate the fault distance in multiterminal HVDC systems. The frequency is estimated using the Hilbert–Huang transform (HHT) and related to the fault distance using a pre-calculated curve. The proposed algorithm was analysed in simulations and deployed in hardware using a digital signal processor (DSP). In the simulation environment, the algorithm was fully selective for faults within the first protection zone and had a correct operation rate of 94% or more for faults located in the second protection zone. In the hardware implementation, in all performed tests, the faults were correctly detected and identified as being internal or external.

The remaining of this paper is organised as follows. Section 2 presents the test system and the distance/frequency relationship. Section 3 briefly discusses the HHT, the core of the proposed algorithm. The complete algorithm is presented in Section 4 and its performance is evaluated using simulations in Section 5. The hardware implementation and further tests in hardware are described in Section 6. Finally, the conclusions are made in Section 7.

2 Distance/frequency relationship

Fig. 1 presents a symmetric monopole modular multilevel converter-based multiterminal HVDC (MMC-MTDC) system with four terminals [29].

The DC voltage during two different pole-to-pole faults at link 14 is presented in Fig. 2. In both cases, the fault resistance was 1 Ω but with different distances of 30and 70 km from MMC 4, respectively. Analysing Fig. 2, it is possible to observe that although the DC voltage collapses, the waviness in both cases had different frequencies. This was due to the effect of the travelling waves through the faulted cable. The greater the distance between the fault and the converter, the longer the time elapsed before the reflected wave reaches the measuring terminal and the more spaced the oscillations of the DC voltage become. Therefore, if the frequency of the DC voltage could be calculated, it would be possible to estimate the fault distance and then localise the fault within a primary or secondary protection zone.

Considering that short-circuit resistance is smaller than the cable characteristic impedance and that converter equivalent impedance is greater than the cable characteristic impedance, the reflected wave in the converter will maintain its polarity until it reaches back to the short-circuit point, when polarity is inverted. Then, the wave will reach the converter terminal with opposite polarity and will be reflected to the fault without changing its polarity. As the polarity is changed only at the fault point, every two travelling wave periods the wave will have its polarity changed. As a complete period is formed of two polarity changes, four travelling wave periods are needed to form a complete DC voltage oscillation. This concept is illustrated in the lattice diagram [30] in Fig. 3, where Γ_A and Γ_F are the reflection coefficients of points A and F, respectively. For the sake of simplicity, only the reflections between the fault (point F) and the converter A were considered.

Therefore, the voltage frequency (f) can be related to distance (d) using the travelling wave speed in the given frequency (ν_f)

$$d = \frac{\nu_f}{4f} \tag{1}$$

However, frequency calculation in DC systems is not as straightforward as in AC systems. In AC systems, the frequency is defined by large electric machines. When a fault occurs, the frequency stays close to the nominal value and the waveforms after the transient period are still close to sinusoidal. Thus, it is possible to use techniques that consider linear systems and stationary signals, such as the discrete Fourier transform (DFT). On the other hand, in DC systems, the frequency of the DC voltage during the fault is not known beforehand, and it is dependent on the distance. Therefore, techniques that deal with non-stationary and non-linear systems must be used in this case. Additionally, as the frequency of oscillation is not known beforehand, the basis used by the frequency extraction technique must be adaptive rather than prefixed. For this reason, the HHT was chosen for frequency extraction. The characteristics of the HHT are discussed in the next section.

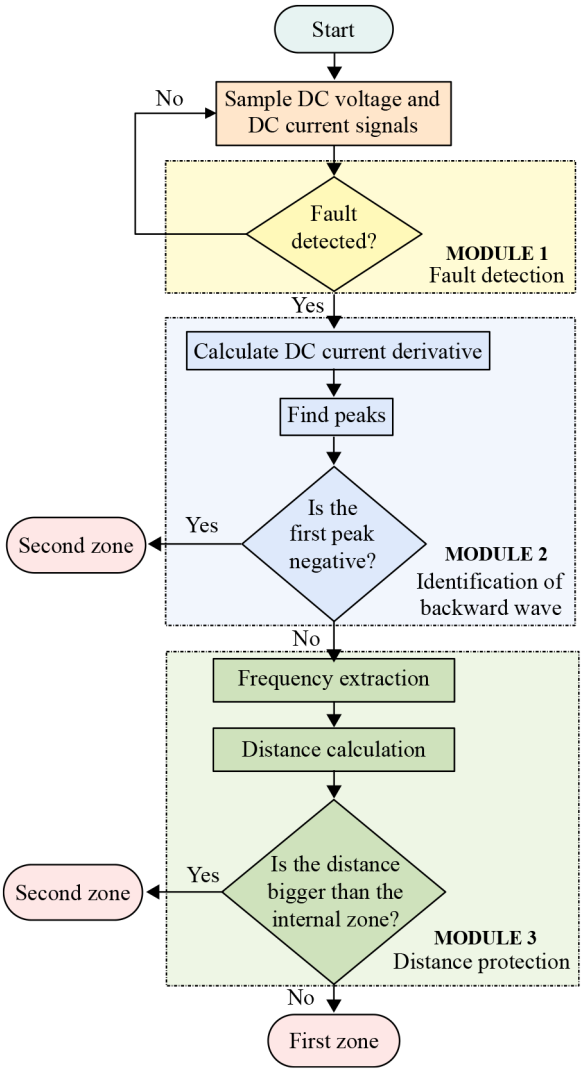

Fig. 4 *Flowchart of the proposed algorithm*

3 Hilbert–Huang transform

The HHT is formed by a joint between the Hilbert transform and the empirical mode decomposition (EMD) proposed by Huang *et al.* [31]. The EMD is a signal decomposition technique that separates a signal in different vibration modes called intrinsic mode functions (IMFs). The EMD looks for local oscillations in the signal and define a local oscillation as the variation in the wave between two local extrema (minimums and maximums). The process of extracting these oscillations was named by Huang *et al.* [31] as the sifting process and can be summarised as follows. Given a signal $x(t)$:

(1) Identify all extrema (minimums and maximums) of $x(t)$.
(2) Interpolate the maximums forming an envelope $\max(t)$. Do the same for minimums ($\min(t)$).
(3) Compute the average $m_1(t) = \max(t) - \min(t))/2$.
(4) Compute the difference $h_1(t) = x(t) - m_1(t)$.
(5) Repeat the same process for k times on $h_1(t)$ until $h_{1k}(t)$ respect the existing conditions.
(6) Store the first IMF $c_1(t) = h_{1k}(t)$
(7) Calculate the first residue $r_1(t) = x(t) - c_1(t)$.
(8) Restart the process treating $r_1(t)$ as the original data.

To be considered an IMF, the signal must respect the existing conditions: (i) the number of extrema and the number of zero crossings are equal or differ at most by one; (ii) $m(t)$ is zero at every point. The decomposition is stopped when either the residue is small or becomes a monotonic function. At the end of the EMD process, it is possible to reconstruct $x(t)$ using the IMFs and the residue

$$x(t) = \sum_{j=1}^{n} c_j(t) + r_n(t) \tag{2}$$

After the EMD, the Hilbert transform is applied separately to each IMF. Being $x(t)$ a real signal, the Hilbert transform ($H[\,.\,]$) of $x(t)$ can be calculated as follows [32]:

$$H[x(t)] = y(t) = \frac{1}{\pi}\int_{-\infty}^{+\infty} \frac{x(\tau)}{t-\tau}\,\mathrm{d}\tau \tag{3}$$

Hence, it is possible to construct an analytic signal using the real and the transformed signals

$$z(t) = x(t) + jy(t) = a(t)\,\mathrm{e}^{j\theta(t)} \tag{4}$$

where $a(t)$ is the signal instantaneous amplitude and $\theta(t)$ is the signal instantaneous phase.

Then, the signal instantaneous frequency $\omega(t)$ is calculated differentiating $\theta(t)$ with respect to time

$$\omega(t) = \frac{\mathrm{d}\theta}{\mathrm{d}t} \tag{5}$$

Thus, using the HHT, it is possible to separate the DC voltage oscillation in different IMFs and calculate the instantaneous frequency of the mode related to the fault travelling waves. As in the proposed algorithm the instantaneous frequency is not the parameter of interest, it is useful to calculate the average frequency using the marginal Hilbert spectrum (MHS(ω)):

$$\mathrm{MHS}(\omega) = \int_0^T H(\omega, t)\,\mathrm{d}t \tag{6}$$

where T is the window size. MHS(ω) provides a measure of the accumulated amplitude in the window for each frequency [33]. It is calculated by summing each frequency value of $H(\omega, t)$ over time. The MHS(ω) shows the total energy that each frequency value contributed along the observed time window. As $H(\omega, t)$ is complex, the phase derivative gives the instantaneous frequency and the absolute value gives the instantaneous amplitude. When the absolute of $H(\omega, t)$ is summed over time, the amplitudes accumulate at the prevalent frequencies. Thus, when the average frequency is taken from the MHS(ω), the value of frequency where the signal had a greater amplitude will have a greater contribution. Therefore, it is possible to extract the amplitude-weighted average frequency in the time window.

4 Proposed protection algorithm

The proposed protection algorithm consists of three modules. The fault detection, the identification of the backward wave and the distance protection. Fig. 4 presents the algorithm flowchart. In all modules, the DC voltage is in p.u. and the DC current derivative is in kA/ms. All variables are sampled at a fixed sampling frequency and the derivative is calculated by dividing the difference between two samples by the sampling interval.

Each module is explained in the following subsections.

4.1 Fault detection

Fault detection is performed using a double criteria: the DC current derivative ($\mathrm{d}I_{\mathrm{dc}}/\mathrm{d}t$) must be higher than a predefined threshold and the DC voltage (V_{dc}) must drop below a predefined value. Both criteria are related to the behaviour of the DC system during the first moments of the fault, when the DC capacitors discharge.

The algorithm in Module 1 (Fig. 5) summarises the fault detection module, where $K_{\mathrm{d}i/\mathrm{d}t}$ and $K_{V\mathrm{dc}}$ are, respectively, the

Data: $K_{didt}, K_{Vdc}, \Delta t_s$
Input: V_{dc}, I_{dc}
Output: Flag: fault detection
begin
  for each sample i **do**
    $\frac{\mathrm{d}I_{dc}}{\mathrm{d}t} \leftarrow (I_{dc}[i+1] - I_{dc}[i])/\Delta t_s$
    if $\frac{\mathrm{d}I_{dc}}{\mathrm{d}t} > K_{didt}$ AND $V_{dc} < K_{Vdc}$ **then**
      Fault detected
    end
  end
end

Fig. 5 *MODULE 1 – Fault detection*

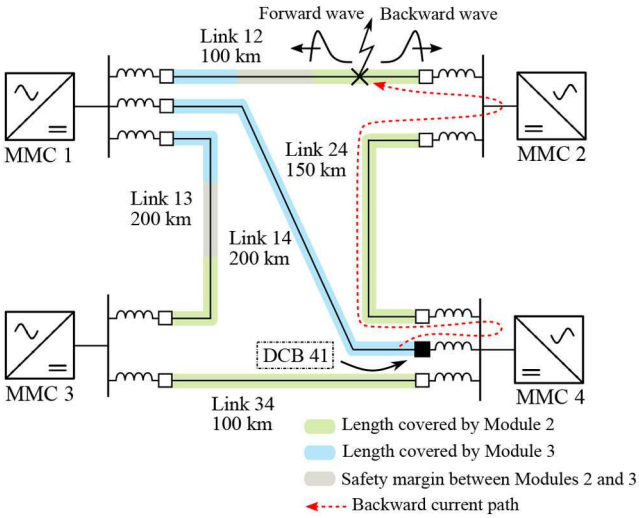

Fig. 6 *Backward current discharging effect and protected areas by Module 2 and Module 3 (Figs. 7 and 8), considering a safety margin in Module 2 (Fig. 7)*

Data: K_{rev}
Input: $\frac{\mathrm{d}I_{dc}}{\mathrm{d}t}$
Output: Flag: backward wave identified
begin
  for each $i \in window$ **do**
    if $\frac{\mathrm{d}I_{dc}}{\mathrm{d}t} > K_{rev}$ **then**
      $id_{pos} \leftarrow i$
    else if $-\frac{\mathrm{d}I_{dc}}{\mathrm{d}t} > K_{rev}$ **then**
      $id_{neg} \leftarrow i$
    end
  end
  if $id_{neg}(1) < id_{pos}(1)$ **then**
    backward wave identified
  end
end

Fig. 7 *MODULE 2 – identification of backward wave*

predefined threshold for the maximum DC current derivative and the minimum DC voltage and Δt_s is the sampling time.

If a DC fault is detected, the algorithm proceeds to the identification of the backward wave.

4.2 Identification of backward wave

The identification of the backward wave module adds selectivity to the protection algorithm. When a fault happens in a meshed DC grid, there are multiple possible paths between the circuit breaker and the fault. There is the path through the cable being protected, called forward wave, and there are also other paths through the other cables, called backward waves. If a backward wave hits the circuit breaker first, the first peak of the current derivative will be negative, because the system discharges in a reverse direction prior to the arrival of the forward wave. If this first peak can be identified, it is certain that the fault happened in other cable/line. The same technique was used by Auran *et al.* [34].

Ideally, the backward wave identification module would cover all external faults whose backward path is shorter than the forward path. If the algorithm is running at Link 14 next to the MMC 4, the backwards-protected lengths would be all of Link 24, all of Link 34, after 25 km from MMC 1 at Link 12 and after 50 km from MMC 1 at Link 13. However, because of oscillations in the current in normal operation and because of the noise, an appropriate safety margin must be selected below which the derivative of current would indicate external fault. The safety margin must be defined higher than the maximum current derivative in normal operation. Thus, this parameter is defined specifically for each MTDC system, where the converters' parameters, control systems, line impedances, line lengths and noise tolerances will indicate the maximum current derivative in normal operation. Fig. 6 depicts the backward current discharging effect, having the circuit breaker DCB 41 as a reference. In the given example of Fig. 6, the fault happened in Link 24. As the path through Link 24 is shorter than the path through Link 24 + Link 12 + Link 14, the backward wave reaches the DCB 41 earlier than the forward wave, resulting in a temporary negative current while the forward wave arrives.

The algorithm in Module 2 (Fig. 7) summarises the backward wave identification module, where K_{rev} is the predefined threshold for backward wave identification.

If a fault is not identified as a backward type, the fault can be either in the protected cable or in another cable close to the protected cable. Therefore, in these cases, the distance of the fault must be estimated in order to operate the circuit breaker correctly.

4.3 Distance protection

The distance protection module aims to estimate the distance between the circuit breaker and the fault. This module receives V_{dc} as input and applies the EMD. Among the IMFs resulted from the EMD, the algorithm chooses just the IMF with the highest RMS value. This is done due to the travelling wave effect being the most significant cause of oscillation on V_{dc} although there are other causes of oscillation such as the DC bus capacitor discharge and the converter discharge. Thus using only the IMF related to the travelling wave effect ensures a major correlation between the calculated frequency and the estimated distance.

The algorithm proceeds calculating the MHS in the time window, and the average frequency is calculated using the MHS centroid. In the centroid calculation, the 20% outliers are removed. The average frequency (ω_{avg}) can be related to distance using (1). However, as the travelling wave speed is also frequency-dependent, a curve that relates distance to frequency can be used. This curve must be adjusted before the operation of the algorithm, using simulations. If the calculated distance is within 90% of the cable length, the fault is classified as in the first protection zone.

The algorithm in Module 3 (Fig. 8) summarises the distance protection module, where $f(P, \omega)$ is the predefined curve that relates the average frequency to distance.

5 Evaluation of the proposed algorithm

In order to evaluate the proposed algorithm, the system presented in Fig. 9 was simulated assuming the circuit breaker responsible for the protection of the Link 14 (DCB 41) as a reference. The system was modelled in PSCAD/EMTDC and its parameters are summarised in Table 2 in the Appendix. The converters were modelled with the detailed Thévenin equivalent model. All DC links were modelled using the frequency-dependent cable model. The cables were 320 kV cross-linked polyethylene (XLPE) insulated. The cables parameters were based on [29]. The armour and sheath were assumed to be ideally grounded, and soil resistivity was assumed to be 1 Ωm. The converter's internal overcurrent protection was set to $2\,\mathrm{p.u.} = 3.87$ kA and the pick-up time was 100 μs.

Data: $f(P, \omega)$
Input: V_{dc}
Output: d

begin
  IMFs ← EMD(V_{dc})
  IMF1 ← greatest(IMFs)
  IMF1 ← IMF1 − mean(IMF1)
  $[a_{inst}, \omega_{inst}]$ ← Hilbert Transform(IMF1)
  $[a_{acum}, \omega_{acum}]$ ← MHS(a_{inst}, ω_{inst})
  ω_{avg} ← centroid(a_{acum}, ω_{acum})
  $d \leftarrow f(P, \omega = \omega_{avg})$
  if $d <$ 90 % of the cable length **then**
    Trip: First zone
  else
    Delayed trip: Second zone
  end
end

Fig. 8 *MODULE 3 – distance protection*

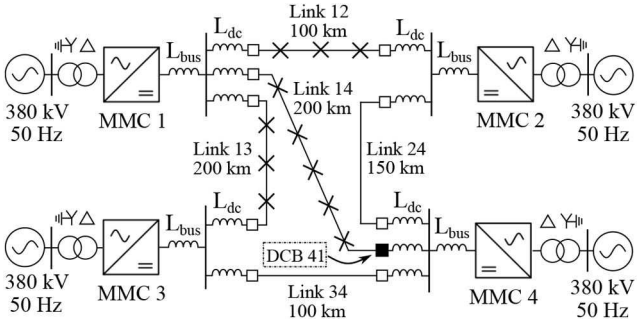

Fig. 9 *MTDC test system used for the algorithm evaluation. Based on [29]*

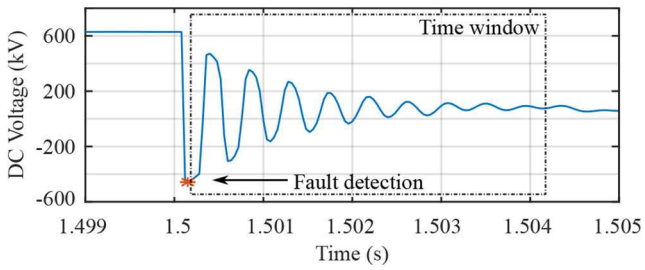

Fig. 10 *DC voltage. Fault 20 km from Link 14*

5.1 Adjustment of the frequency × distance curve

It was verified in (1) that frequency and distance have an inverse relation. Therefore, the function used to model their relation was

$$d = \frac{p_1}{\omega_{avg} + p_2} + p_3 \tag{7}$$

For adjustment of the $f(P, \omega)$ curve, 1 Ω pole-to-pole faults on Link 14 from 10 to 200 km in steps of 10 km were applied. In these cases, the distance between the fault and DCB 41 was known beforehand, and the average frequency extracted from the distance module was related to the real fault location. After interpolation, $f(P, \omega)$ was formed. The $f(P, \omega)$ curve does not change if there is a network topology change. As in the proposed scheme, each line is protected by a dedicated DC circuit breaker at both ends, and so each local protection would be adjusted considering the characteristics of the line being protected. This invariability can be explained by the presence of DC inductors at the end of each line, which is a natural barrier against the travelling waves from the other lines.

Fig. 10 shows an example of a fault simulated 20 km from DCB 41. The IMFs extracted from EMD are presented in Figs. 11 and 12 show the instantaneous frequencies. The MHS is presented in Fig. 13. Although the accumulated frequencies for all IMFs were plotted together in Fig. 13, they were obtained separately for each IMF and the MHS can be calculated just for the desired IMF. The interpolated curve is presented in Fig. 14, considering the travelling wave speed constant and equal to 183.5 km/ms for the theoretical curve. The code used for EMD was based on [35].

5.2 Parameters

The algorithm parameters were defined through simulation. The size of the time window must be chosen according to the maximum time allowed by the DC circuit breakers supportability and by the length of the protected line/cable. In the system presented in Fig. 9, the length of Link 14 is 200 km. As the travelling wave speed through the simulated cables is 183.5 km/ms, the travelling wave delay is 1.09 ms for 200 km. Thus, it takes $4 \cdot 0.98 = 3.92$ ms to form one period in the voltage oscillation if a fault happens at the most distant part of the protected cable (90% of 200 km). Therefore, the window length was chosen as 4 ms. This means that for distant faults (farther than 180 km), the algorithm will process an incomplete period. Even so, calculating the average frequency will still provide a low error fault location. The choosen parameters were sampling frequency = 50 kHz, $K_{\mathrm{d/dt}} = 0.85$ kA/ms, $K_{V\mathrm{dc}} = 1.0$ p . u, $K_{\mathrm{rev}} = 0.1$ kA/ms.

5.3 Overall result

To check the performance of the proposed algorithm, 1 Ω pole-to-pole faults were applied on Link 14 from 15 to 185 km in steps of 10 km, on Link 12 from 0 km to 90 km in steps of 5 km and on Link 13 from 0 km to 190 km in steps of 10 km. Table 3 in the Appendix summarises the algorithm performance, showing Modules 1, 2 and 3 (Figs. 5, 7, 8) trips, the calculated frequency and distance when Module 3 was run 8, and the protection zone.

From Table 3, it is possible to observe that all faults that occurred in Link 14 were classified correctly. The fault that occurred at 185 km was classified as in the second zone, although this was a proper operation according to the defined boundary of 90% of the cable. It can also be observed that only a few Hz separate the first to the second zone, which underscores the challenge of the selective operation. Nevertheless, if a DFT with 4 ms window was used, the resolution would be in harmonics of 250

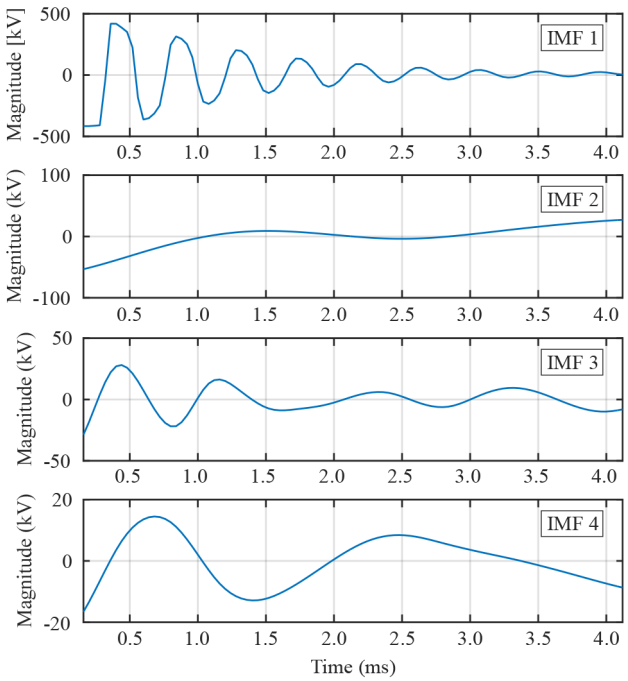

Fig. 11 *IMFs obtained from EMD. Fault 20 km from Link 14*

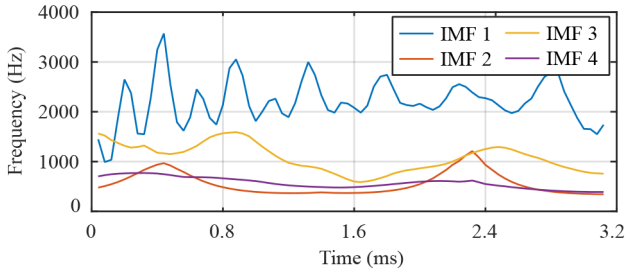

Fig. 12 *Instantaneous frequency of the IMFs*

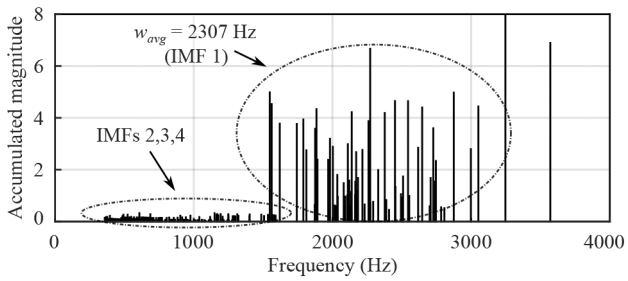

Fig. 13 *MHS of the IMFs*

Hz, given errors around 100 km. On the other hand, the technique used here provided a resolution of a few Hz, with errors smaller than 10 km.

The algorithm operated improperly in the cases where the fault occurred next to the middle of adjacent cables (fault 40 km at Link 12 and 70 km at Link 13), where the backward algorithm could not trip, and the similar distance between both forward and backward paths and the breaker led to an inaccurate operation.

Finally, it could be observed that 100% of Link 14, 94% of Link 12 and 95% of Link 13 were correctly and selectively protected for the cases tested, which reveals a high selectivity level of the proposed algorithm, even without any communication between terminals or between circuit breakers in the same terminal.

6 Hardware implementation

In order to verify the applicability of the proposed technique, the complete algorithm was embedded and tested in hardware running in real-time.

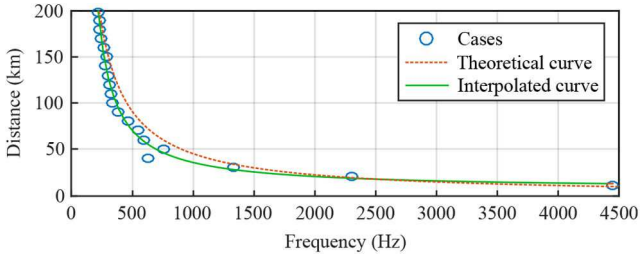

Fig. 14 *Adjusted frequency × distance curve*

The algorithm was embedded in a TMS320F28379D Dual-Core Delfino™ Digital Signal Controller (DSC) from Texas Instruments. The DSC pins were accessed through a TMDSDOCK28379D Experimenter Kit. Two 12-bit analogue-to-digital converters (ADCs) were used to sample the DC voltage and DC current, providing a resolution of 4096 levels. The algorithm was running at a sampling frequency of 25 kHz. The voltage limits of the ADCs were 0–3.3 V. Additionally, two 12-bit digital-to-analogue converters (DACs) were used to reproduce the computed IMFs from the DSC.

The faulted voltage and current waveforms were generated by analogue voltage signals between 0 and 3 V using a Digilent Analogue Discovery 2 oscilloscope/signal generator. The same oscilloscope was used to read the digital outputs from the DSC, containing the protection trips, processing times and the analogue outputs containing the calculated IMFs. As the oscilloscope is controlled by PC, the waveforms were generated after a trigger was received. The trigger signal was generated using one of the oscilloscopes digital outputs, commanded by PC. The triggered operation ensured that the generated waveforms were synchronised and that the test start time could be known. The DSC digital outputs were: fault detection trip (Module 1 (Fig. 5)), external fault flag (Module 2 (Fig. 7)), possible internal fault flag (Module 2 (Fig. 7)), EMD elapsed time (Module 3), Hilbert transform elapsed time (Module 3), external fault flag (Module 3), internal fault trip (Module 3) and the calculated distance (Module 3) (Fig. 8). The calculated distance was displayed in the digital output in the following manner: the DSC pin was set high for 0.1 ms per km. Due to the oscilloscope limitation of only two channels, only two IMFs were acquired from the DACs of the DSC per test. The exchanged signals between the oscilloscope and the DSC are depicted in Fig. 15 and the experiment setup is presented in Fig. 16.

Besides the intrinsic noise present in the process of generating the waveforms and converting to digital values, an additional Gaussian noise was introduced in the generated signals, with SNR of 40 dB, in order to test the algorithm robustness. After conversion, the variables were filtered. As the frequency of V_{dc} is critical for the distance calculation, it was filtered only by a moving average filter of two samples. As the derivative amplifies the noise, I_{dc} was filtered using a sixth-order Butterworth filter with a cutting frequency of 2.5 kHz.

In order to adjust the algorithm for use in hardware, some adaptations were made. First, the computational effort to execute the algorithm was shared between the two processors of the DSC, with one processor sampling and filtering the signal and the other processor running the protection modules. The sampling frequency was reduced to 25 kHz. In the second module, the current derivative margin was raised to $K_{rev} = 0.7$ kA/ms to ensure safe external fault identification even with the noise. The start of the 4 ms window for the voltage was given when the DC voltage crossed 0.85 p.u. In the third module, the Hilbert transform was implemented using a 64-sample length FIR filter. The average frequency was obtained just by the simple mean of the frequency spectrum, instead of the centroid of the MHS. Instead of using only the IMF 1, the IMFs with RMS value higher than 30 kV was summed, in order to avoid mode mixing and the noise. The frequency was related to distance just by multiplication of the travelling wave speed (183.5 km/ms). The EMD was implemented based on [31] and performed with 20 fixed iterations per IMF. A maximum of three IMFs were extracted.

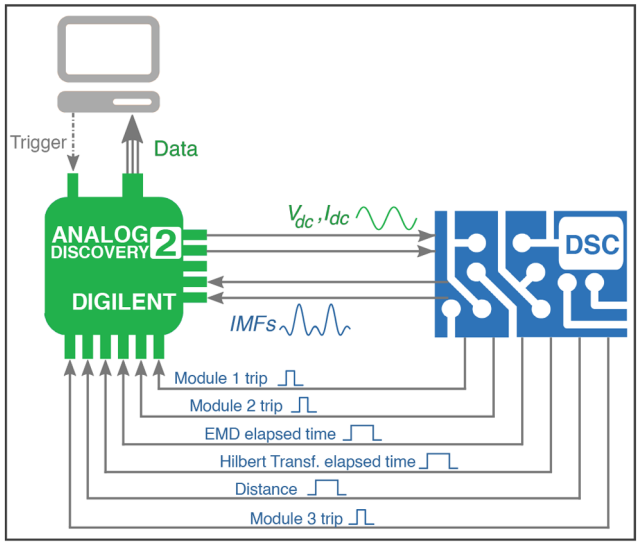

Fig. 15 *Experiment schematic diagram*

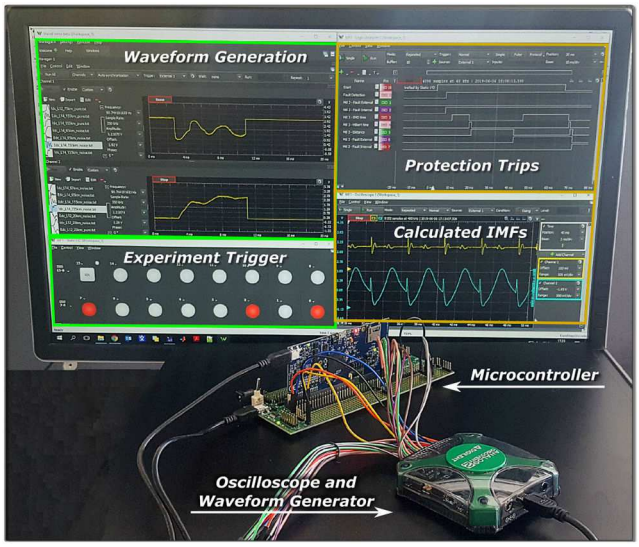

Fig. 16 *Experiment setup*

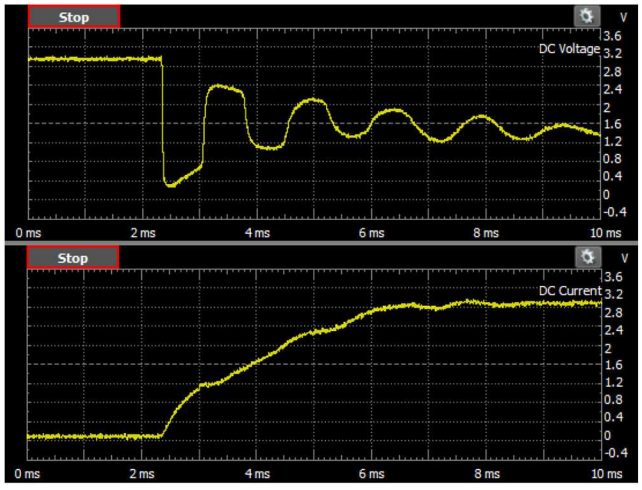

Fig. 17 *Test 1 – generated waveforms*

Three fault tests were performed. The first was at Link 14, 65 km from the MMC 4. The second was at Link 12, 20 km from the MMC 1. The third was at Link 13, 120 km from the MMC 1. These tests enabled the verification of the performance of the algorithm by discriminating between internal and external faults using the second and third modules.

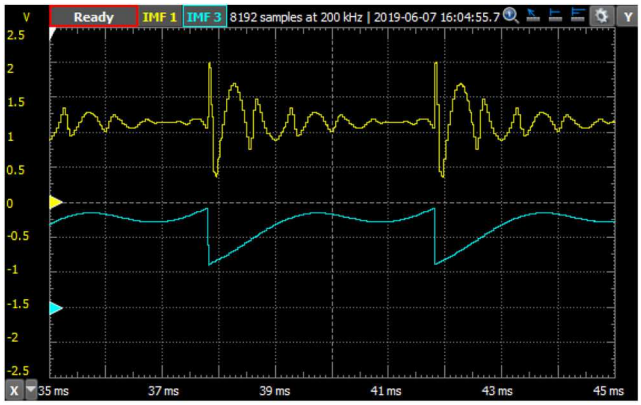

Fig. 18 *Test 1 – IMF 1 and IMF 3*

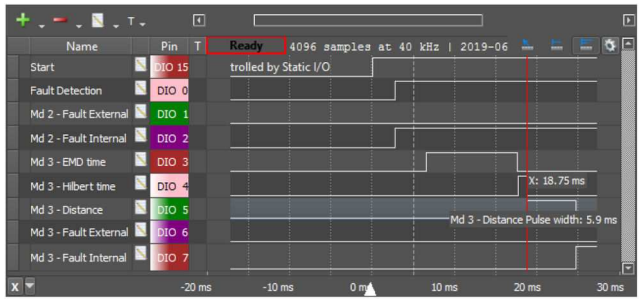

Fig. 19 *Test 1 – protection triggers and elapsed times*

6.1 Test 1 – link 14, 65 km

The first test was an internal fault 65 km from the DCB 41. Fig. 17 shows the generated signals for V_{dc} and I_{dc}. The noise presented in the signals can be clearly seen. It should be noted that the noise presented in Fig. 17 is only due to the artificially added noise with SNR of 40 dB, but others sources of noise are present in the signal generation, from the signal generator to the A/D conversion and during the A/D conversion. Thus the total noise could only be seen after the complete signal A/D conversion.

Fig. 18 shows the IMF 1 and IMF 3. An offset of -1.5 V was given to the second channel (IMF 3) in blue to facilitate the visualisation of both waveforms. As the sampling window was 4 ms of data, the waveforms shown repeat each 4 ms. The IMF 1 had a higher frequency comparing to the IMF 3, due to the nature of the EMD of sifting higher frequency modes first.

The algorithm elapsed times and protection trips are shown in Fig. 19. It can be observed that a few milliseconds after the test start, the fault is detected. This is due to the portion of the pre-fault samples present in the generated signals. After the fault was detected, the detection trip started Module 2 (Fig. 7), and the fault was classified as possibly internal. This classification triggered Module 3 (Fig. 8), which applied the EMD to the given signal. The EMD processing time was 10.97 ms. After the EMD, the Hilbert transform was applied to the selected IMF, which took 1.08 ms to operate. After the average frequency being calculated, it was multiplied by the travelling wave speed resulting in a distance of 59 km (5.9 ms of pulse width). As the calculated distance was smaller than 90% of the length of the cable, the fault was correctly identified as internal (first protection zone).

6.2 Test 2 – link 12, 20 km

The second test was an external fault 20 km from the MMC 1 and 220 km from the DCB 41. Fig. 20 shows the generated signals for V_{dc} and I_{dc}. Fig. 21 shows the IMF 2 and IMF 3. As the frequency of the mode of oscillation related to the fault was smaller, the first IMF 1 was composed only by the noise (the highest frequency). The IMF 2 was amplified five times in the oscilloscope to facilitate the visualisation. It can be seen from the IMF 3 that despite the V_{dc} signal being contaminated with noise, the EMD played an important role in removing the high-frequency noise, as this

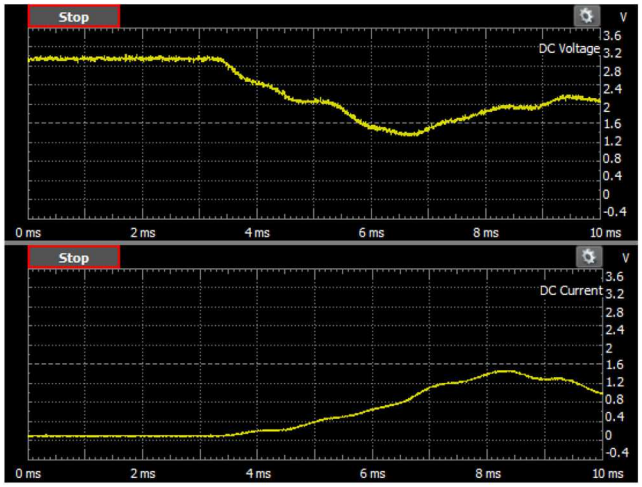

Fig. 20 *Test 2 – generated waveforms*

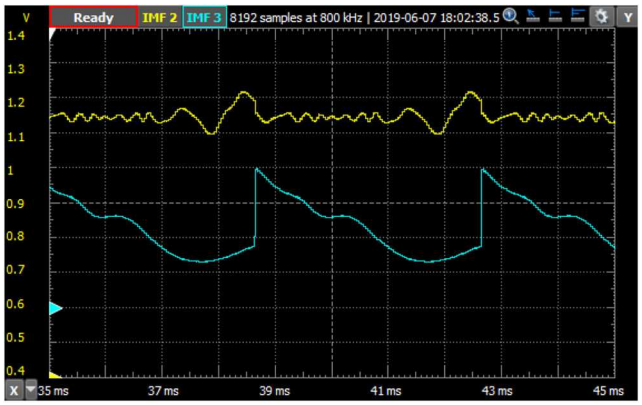

Fig. 21 *Test 2 – IMF 1 and IMF 3*

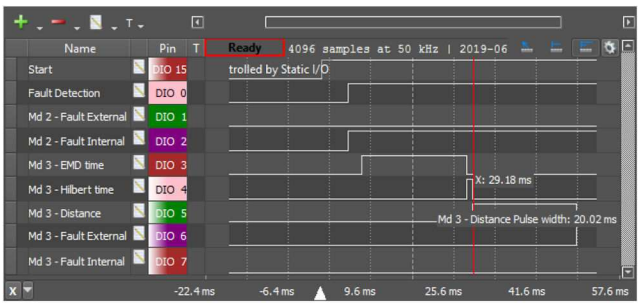

Fig. 22 *Test 2 – protection triggers and elapsed times*

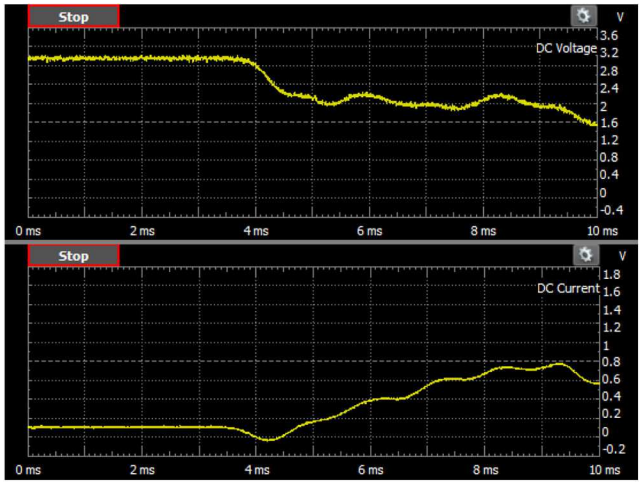

Fig. 23 *Test 3 – generated waveforms*

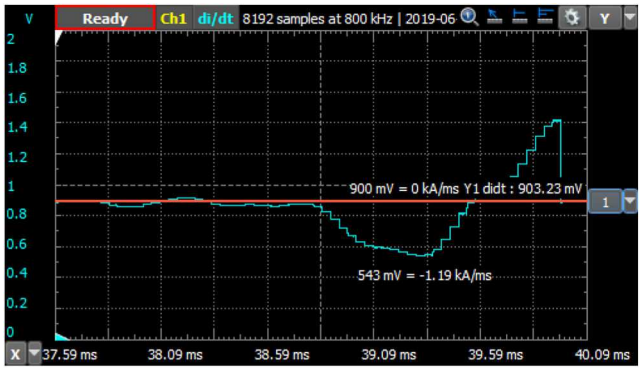

Fig. 24 *Test 3 – current derivative*

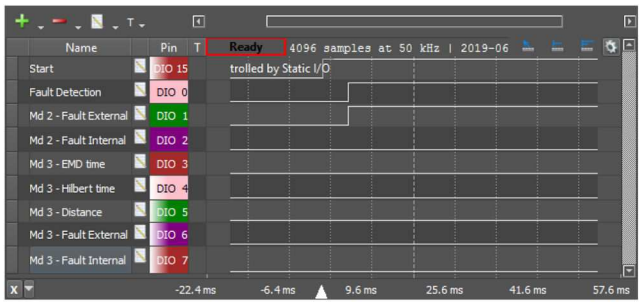

Fig. 25 *Test 3 – protection triggers and elapsed times*

contamination could bias the frequency spectrum resulting in an average frequency higher than the correct.

The protection trips are shown in Fig. 22. Although the Module 2 (Fig. 7) classified the fault as potentially internal, Module 3 (Fig. 8) calculated a distance of 200.2 km (20.02 ms of pulse width). As the calculated distance was greater than 90% of the length of the cable, the fault was correctly identified as external (second protection zone). The actuation of the Module 2 (Fig. 7) was correct even showing a possible internal fault because the distance forwards through Link 12+ Link 14 was smaller than the distance backwards through Link 12 + Link 24. Thus, in this condition, the derivative would not be negative prior to being positive to indicate an external fault. In this case, the final decision was made by Module 3 (Fig. 8). The processing times were 20 ms for the EMD and 1.08 ms for the Hilbert transform.

6.3 Test 3 – link 13, 120 km

The third test was also an external fault, but now at Link 13, 120 km from the MMC 1. The fault was located 320 km forward (Link 13 + Link 14) and 180 km backward (Link 13 + Link 34) from the DCB 41. Fig. 23 shows the generated signals for V_{dc} and I_{dc}. As this fault was successfully identified as external, Module 3 (Fig. 8) was not performed. Instead of the IMFs, the current derivative was output to confirm Module 2 operation (Fig. 7). As can be observed in Fig. 24, the current derivative was around zero during the pre-fault condition (the zero line was indicated by a red line). When the fault happened, the backward wave reached the MMC 4 backwards before reaching forwards, which caused the current derivative to be negative before being positive. As the derivative was below the margin of −0.7 kA, the fault was identified as external, as can be seen in Fig. 25.

6.4 Discussion

In the three tests presented, the proposed algorithm performed according to the desired operation, successfully detecting all the faults (Module 1 (Fig. 5)), identifying external faults by backward waves (Module 2 (Fig. 7)) and identifying internal and external faults using the estimated distance (Module 3 (Fig. 8)).

The implementation in hardware required a few adaptations from the simulated algorithm. However, even with the adaptations, the algorithm performed correctly, and the distance error was

around 10% in both cases. The higher error compared to the simulation was possibly caused by a sum of reasons including the low sampling frequency, the noise, the A/D quantisation errors and the simple average in the frequency calculation. However, even with these sources of error, the algorithm performed correctly, with no communication between terminals or between circuit breakers in the same terminal. The algorithm precision is considered satisfactory taking into account that the primary goal of the proposed protection algorithm is to define the line in fault, not to precisely localise the fault. Precise fault locations will be given by dedicated algorithms, which usually require communication and operate after the fault is identified.

The total algorithm processing time in the selected embedded hardware was 12 ms in the first test, 21 ms in the second test and 970 μs in the third test. As the algorithm uses 4 ms for filling the sampling window, the trip should be given not more than a few milliseconds later, to reduce the circuit breaker requirements. According to this, the proposed algorithm should process the data one order of magnitude faster. However, it is worth noting that the algorithm was embedded in a simple digital signal controller and that the necessary speed increase should be reached using FPGAs or other more powerful hardware. Despite that, the tests performed showed that even performing a total of 60 iterations in the EMD process (extrema finding and spline interpolation), the technique was processed fast enough to indicate that the technique could be used in real-world applications.

7 Conclusions

The protection of multiterminal HVDC systems is still a challenge for the industry and research community. Correctly and selectively identifying the faulty cable/line without the need of communication between terminals is one of the challenges that must be overcome in order to operate the grid with reliability [13].

In this context, distance protection, commonly used in AC systems, can be translated to DC and play a significant role, adding selectivity to existing detection algorithms. As impedance-based distance protection cannot be used in DC systems, previous works have used other variables such as the cable resistance and the resolution of differential equations. However, some techniques do not present the speed requirement for VSC-HVDC systems or need communication between terminals.

Therefore, the present work proposed the use of the frequency of the DC voltage transient oscillation to estimate the fault distance. The frequency was estimated using the HHT and was then compared with a pre-defined curve. In the simulations, the algorithm was fully selective for faults within the first protection zone and had a correct operation rate of 94% or more for faults located in the second zone. Furthermore, the algorithm presented a low average error for distance estimation.

The algorithm was implemented in hardware, and three tests were performed in real-time. In all tests, the fault was correctly detected and identified as being internal or external. The distance was calculated with an error of 10% even in the presence of noise and without any communication between terminals or between circuit breakers in the same terminal.

The results confirmed the potential of signal processing in distance protection algorithms and indicated that the proposed algorithm could be used in real-world applications, in conjunction with fault detection techniques, adding selectivity to multiterminal DC protection schemes.

8 Acknowledgments

The authors acknowledge the University of Strathclyde, UK and the University of São Paulo, São Carlos, Brazil for the facilities provided. The authors' thank also to the São Paulo Research Foundation (FAPESP), grant no. [2018/10667-6] for funding this research.

9 References

[1] Hertem, D.V., Gomis-Bellmunt, O., Liang, J. (Eds.): '*HVDC grids – for offshore and supergrid of the future*' (John Wiley & Sons, Inc., Hoboken, NJ, USA, 2016)

[2] Gordon, S.: 'Supergrid to the rescue [electricity supply security]', *Power Eng.*, 2006, **20**, (5), p. 30

[3] Buijs, P., Bekaert, D., Cole, S., *et al.*: 'Transmission investment problems in europe: going beyond standard solutions', *Energy Policy*, 2011, **39**, (3), pp. 1794–1801

[4] Jovcic, D., Ahmed, K.: '*High voltage direct current transmission: converters, systems and DC grids*' (John Wiley & Sons, Chichester, UK, 2015)

[5] Häfner, J., Jacobson, B.: 'Proactive hybrid hvdc breakers-a key innovation for reliable hvdc grids'. Integrating supergrids and microgrids Int. Symp., CIGRE, Bologna, 2011

[6] Kerf, K.D., Srivastava, K., Reza, M., *et al.*: 'Wavelet-based protection strategy for DC faults in multi-terminal VSC HVDC systems', *IET Gener. Transm. Distrib.*, 2011, **5**, (4), p. 496

[7] Leterme, W., Van-Hertem, D.: 'Classification of fault clearing strategies for hvdc grids'. Across Borders-HVDC Systems and Markets Integration, CIGRE, Lund, 2015

[8] Farhadi, M., Mohammed, O.A.: 'Protection of multi-terminal and distributed DC systems: design challenges and techniques', *Electr. Power Syst. Res.*, 2017, **143**, pp. 715–727

[9] Wang, J., Berggren, B., Linden, K., *et al.*: 'Multi-terminal dc system line protection requirement and high speed protection solutions'. Across Borders–VDC Systems and Market Integration, CIGRE, Lund, 2015

[10] Zou, G., Feng, Q., Huang, Q., *et al.*: 'A fast protection scheme for VSC based multi-terminal DC grid', *Int. J. Electr. Power Energy Syst.*, 2018, **98**, pp. 307–314

[11] Sneath, J., Rajapakse, A.D.: 'Fault detection and interruption in an earthed HVDC grid using ROCOV and hybrid DC breakers', *IEEE Trans. Power Deliv.*, 2016, **31**, (3), pp. 973–981

[12] Yeap, Y.M., Geddada, N., Ukil, A.: 'Capacitive discharge based transient analysis with fault detection methodology in DC system', *Int. J. Electr. Power Energy Syst.*, 2018, **97**, pp. 127–137. Available at https://doi.org/10.1016

[13] CIGRE Working Group B4-52: 'Technical Brochure 533: HVDC Grid Feasibility Study'. CIGRE, 2013

[14] Chaudhuri, N.R., Chaudhuri, B., Majumder, R., *et al.*: '*Multi-terminal direct-current grids*' (John Wiley & Sons, Inc., Hoboken, NJ, USA, 2014)

[15] Leterme, W., Beerten, J., Hertem, D.V.: 'Nonunit protection of HVDC grids with inductive DC cable termination', *IEEE Trans. Power Deliv.*, 2016, **31**, (2), pp. 820–828

[16] Li, C., Gole, A.M., Zhao, C.: 'A fast DC fault detection method using DC reactor voltages in HVdc grids', *IEEE Trans. Power Deliv.*, 2018, **33**, (5), pp. 2254–2264

[17] Bertho, R., Lacerda, V.A., Monaro, R.M., *et al.*: 'Selective nonunit protection technique for multiterminal VSC-HVDC grids', *IEEE Trans. Power Deliv.*, 2018, **33**, (5), pp. 2106–2114

[18] Li, R., Xu, L., Yao, L.: 'DC fault detection and location in meshed multiterminal HVDC systems based on DC reactor voltage change rate', *IEEE Trans. Power Deliv.*, 2017, **32**, (3), pp. 1516–1526

[19] Huang, Q., Zou, G., Wei, X., *et al.*: 'A non-unit line protection scheme for MMC-based multi-terminal HVDC grid', *Int. J. Electr. Power Energy Syst.*, 2019, **107**, pp. 1–9

[20] Jamali, S., Mirhosseini, S.S.: 'Protection of transmission lines in multi-terminal HVDC grids using travelling waves morphological gradient', *Int. J. Electr. Power Energy Syst.*, 2019, **108**, pp. 125–134

[21] Christopoulos, C., Wright, A.: '*Electrical power system protection*' (Springer, US, 1999)

[22] Horowitz, S.H., Phadke, A.G.: '*Power system relaying*' (John Wiley & Sons, Ltd, Chichester, UK, 2008)

[23] Yang, J., Fletcher, J.E., O'Reilly, J.: 'Multiterminal DC wind farm collection grid internal fault analysis and protection design', *IEEE Trans. Power Deliv.*, 2010, **25**, (4), pp. 2308–2318

[24] Suonan, J., Zhang, J., Jiao, Z., *et al.*: 'Distance protection for HVDC transmission lines considering frequency-dependent parameters', *IEEE Trans. Power Deliv.*, 2013, **28**, (2), pp. 723–732

[25] He, Z., Liao, K., Li, X., *et al.*: 'Natural frequency-based line fault location in HVDC lines', *IEEE Trans. Power Deliv.*, 2014, **29**, (2), pp. 851–859

[26] Tunnerhoff, P., Petino, C., Battiato, M., *et al.*: 'Distance protection for HVDC transmission lines based on MMC modulation strategy'. 2016 Electric Power Quality and Supply Reliability (PQ), Tallinn, Estonia, 2016

[27] Leterme, W., Hertem, D.V.: 'Cable protection in HVDC grids employing distributed sensors and proactive HVDC breakers', *IEEE Trans. Power Deliv.*, 2018, **33**, (4), pp. 1981–1990

[28] Yang, Q., Blond, S.L., Aggarwal, R., *et al.*: 'New ANN method for multi-terminal HVDC protection relaying', *Electr. Power Syst. Res.*, 2017, **148**, pp. 192–201

[29] Leterme, W., Ahmed, N., Hertem, D.V., *et al.*: 'A new HVDC grid test system for HVDC grid dynamics and protection studies in EMT-type software'. 11th IET Int. Conf. on AC and DC Power Transmission, Birmingham, UK, 2015

[30] Bewley, L.V.: 'Traveling waves on transmission systems', *Trans. Am. Inst. Electr. Eng.*, 1931, **50**, (2), pp. 532–550

[31] Huang, N.E., Shen, Z., Long, S.R., *et al.*: 'The empirical mode decomposition and the hilbert spectrum for nonlinear and non-stationary time series analysis', *Proc. R. Soc. A, Math. Phys. Eng. Sci.*, 1998, **454**, (1971), pp. 903–995

[32] Hlawatsch, F., Auger, F. (Eds.): '*Time-frequency analysis*' (ISTE e John Wiley & Sons, Hoboken, NJ, USA, 2008)

[33] Huang, N.E., Wu, Z.: 'A review on Hilbert–Huang transform: method and its applications to geophysical studies', *Rev. Geophys.*, 2008, **46**, (2), pp. 1–23
[34] Auran, G., Descloux, J., Nguefeu, S., *et al.*: 'Non-unit full selective protection algorithm for MTDC grids'. 2017 IEEE Power & Energy Society General Meeting, Chicago, IL, USA, 2017
[35] Flandrin, P., Rilling, G., Goncalves, P.: 'Empirical mode decomposition as a filter bank', *IEEE Signal Process. Lett.*, 2004, **11**, (2), pp. 112–114

10 Appendix

The test system parameters are summarised in Table 2. The algorithm performance via simulations is summarised in Table 3, where ω_{avg} is the average frequency in Hz.

Table 2 MTDC system parameters.

	MMC 1, 2, 3	MMC 4	
AC grid			
AC reactance	17.75	13.34	Ω
AC resistance	1.77	1.34	Ω
Transformer			
power	900	1200	MVA
leakage reactance	0.15	0.15	p.u.
winding voltages	400/400	400/400	kV/kV
Converter			
voltage	380	380	kV
power	900	1200	MVA
SM per arm (N)	50	50	
SM capacitance	1465	1950	μF
arm inductance (L_{arm})	84.8	63.6	mH
SM ON-state resistance	0.0177	0.0134	Ω
SM OFF-state resistance	100	100	MΩ
DC bus			
DC bus reactor (L_{bus})	10	10	mH
DC capacitor (C_{bus})	2.5	2.5	μF
DC line reactor (L_{dc})	30	50	mH

Table 3 Performance of the proposed algorithm

Link	Fault location, km	Fault detection	Backward wave	ω_{avg}, Hz	Estimated distance,km	Error%	Zone	Correct operation
Link 14	15	✓	✗	3009	15.3	0.2	1st zone	✓
	25	✓	✗	1674	23	1.0	1st zone	✓
	35	✓	✗	1181	30.5	2.3	1st zone	✓
	45	✓	✗	1007	35	5.0	1st zone	✓
	55	✓	✗	744	46.5	4.3	1st zone	✓
	65	✓	✗	571	60.6	2.2	1st zone	✓
	75	✓	✗	508	68.6	3.2	1st zone	✓
	85	✓	✗	414	86.2	0.6	1st zone	✓
	95	✓	✗	363	100.4	2.7	1st zone	✓
	105	✓	✗	324	115.3	5.2	1st zone	✓
	115	✓	✗	315	119.5	2.2	1st zone	✓
	125	✓	✗	309	122.8	1.1	1st zone	✓
	135	✓	✗	289	133.7	0.7	1st zone	✓
	145	✓	✗	275	142.7	1.2	1st zone	✓
	155	✓	✗	274	143.7	5.7	1st zone	✓
	165	✓	✗	250	163.1	1.0	1st zone	✓
	175	✓	✗	239	174.1	0.5	1st zone	✓
	185	✓	✗	222	193	4.0	2nd zone	✓
Link 12	0	✓	✗	177	278	—	2nd zone	✓
	10	✓	✗	182	267	—	2nd zone	✓
	15	✓	✗	192	244	—	2nd zone	✓
	20	✓	✗	194	238.3	—	2nd zone	✓
	25	✓	✗	200	227	—	2nd zone	✓
	30	✓	✗	203	221.8	—	2nd zone	✓
	35	✓	✗	227	187.3	—	2nd zone	✓
	40	✓	✗	259	154.6	—	1st zone	✗
	45	✓	✗	216	201	—	2nd zone	✓
	50	✓	✗	229	184.5	—	2nd zone	✓
	55	✓	✓	—	—	—	2nd zone	✓
	60	✓	✓	—	—	—	2nd zone	✓

Link	Fault location, km	Fault detection	Backward wave	ω_{avg}, Hz	Estimated distance,km	Error%	Zone	Correct operation
Link 12	65	✓	✓	—	—	—	2nd zone	✓
	70	✓	✓	—	—	—	2nd zone	✓
	75	✓	✓	—	—	—	2nd zone	✓
	80	✓	✓	—	—	—	2nd zone	✓
	85	✓	✓	—	—	—	2nd zone	✓
	90	✓	✓	—	—	—	2nd zone	✓
Link 13	0	✓	✗	209	212.4	—	2nd zone	✓
	10	✓	✗	213	206.4	—	2nd zone	✓
	20	✓	✗	208	214	—	2nd zone	✓
	30	✓	✗	205	218.8	—	2nd zone	✓
	40	✓	✗	228	186	—	2nd zone	✓
	50	✓	✗	192	242.5	—	2nd zone	✓
	60	✓	✗	218	199.1	—	2nd zone	✓
	70	✓	✗	283	137.3	—	1st zone	✗
	80	✓	✓	—	—	—	2nd zone	✓
	90	✓	✓	—	—	—	2nd zone	✓
	100	✓	✓	—	—	—	2nd zone	✓
	110	✓	✓	—	—	—	2nd zone	✓
	120	✓	✓	—	—	—	2nd zone	✓
	130	✓	✓	—	—	—	2nd zone	✓
	140	✓	✓	—	—	—	2nd zone	✓
	150	✓	✓	—	—	—	2nd zone	✓
	160	✓	✓	—	—	—	2nd zone	✓
	170	✓	✓	—	—	—	2nd zone	✓
	180	✓	✓	—	—	—	2nd zone	✓
	190	✓	✓	—	—	—	2nd zone	✓